

A Pilot Study of Interplanetary Scintillation with FAST

Li-Jia Liu,^{1,*} Bo Peng,^{1,†} Lei Yu,^{1,2,‡} Ye-Zhao Yu,³ Ji-Guang Lu,¹ Bin Liu,^{1,§} O. Chang,⁴ M. M. Bisi,⁴
the FAST Collaboration¹

¹CAS Key Laboratory of FAST, National Astronomical Observatories, Chinese Academy of Sciences, Beijing 100101, China

²University of Chinese Academy of Sciences, Beijing, 100049, China

³School of Physics and Electronics, Qiannan Normal University for Nationalities, Duyun, 558000, China

⁴RAL Space, United Kingdom Research and Innovation - Science and Technology Facilities Council - Rutherford Appleton Laboratory, Harwell Campus, Oxfordshire, OX11 0QX, UK

Accepted 2021 April 20. Received 2021 April 19; in original form 2020 October 01

ABSTRACT

Observations of Interplanetary Scintillation (IPS) are an efficient remote-sensing method to study the solar wind and inner heliosphere. From 2016 to 2018, some distinctive observations of IPS sources like 3C 286 and 3C 279 were accomplished with the Five-hundred-meter Aperture Spherical radio Telescope (FAST), the largest single-dish telescope in the world. Due to the 270–1620 MHz wide frequency coverage of the Ultra-Wideband (UWB) receiver, one can use both single-frequency and dual-frequency analyses to determine the projected velocity of the solar wind. Moreover, based on the extraordinary sensitivity owing to the large collecting surface area of FAST, we can observe weak IPS signals. With the advantages of both the wider frequency coverage and high sensitivity, also with our radio frequency interference (RFI) mitigation strategy and an optimized model-fitting method developed, in this paper, we analyze the fitting confidence intervals of the solar wind velocity, and present some preliminary results achieved using FAST, which points to the current FAST system being highly capable of carrying out observations of IPS.

Key words: scattering – methods: data analysis – sun: solar wind – sun: heliosphere

1 INTRODUCTION

While coming through the solar wind plasma, the radio signal from a distant compact radio source is scattered by the density inhomogeneities of the solar wind, consequently a random diffraction pattern is observed at Earth, this phenomenon is known as Interplanetary Scintillation (IPS) (Hewish et al. 1964). In turn, these ground-based IPS observations can be used to infer the physical properties of the solar wind. Nowadays, as the space-exploration and technologies are growing, the solar-activity monitoring and the space-weather forecasting are becoming more critical. Although the solar wind can be observed directly using an *in-situ* satellite/spacecraft with relatively-high accuracy, the ground-based observations of IPS provide a more economic method to obtain the information of the solar wind, such as velocity as well as the structure of a sub-arcsecond scale compact radio source (Hewish & Symonds 1969; Armstrong & Coles 1972). Another advantage of observations of IPS is that the solar wind can be monitored with a longer time scale and a more flexible spatial range out of the ecliptic

plane. Besides solar physics, observations of IPS can also be used to study space weather.

Since the IPS phenomenon was discovered in the 1960s (Clarke 1964; Hewish et al. 1964), many countries including the UK, USA, Japan, India and, Russia, have undertaken IPS studies. Some astronomical instruments were built exclusively for IPS observations, like the multi-station system in Japan (Asai et al. 1995). Another successful example is called the Ooty Radio Telescope (ORT) located in India (Manoharan & Ananthakrishnan 1990). The two facilities are both based on a parabolic cylinder design using a central observing frequency of 327 MHz. Since observations of IPS are an effective way to study heliospheric physics, some new facilities for IPS studies have been built or are going to be built, like the Mexican Array Radio Telescope (MEXART) (Mejia-Ambriz et al. 2010; Chang et al. 2016) in Mexico, and a new IPS telescope system to be constructed in Inner Mongolia, China, which is an array with three 140*40 m cylinder antennas at Mingantu, together with two 16 m parabolic antennas at Abaga and Keshiketeng (Yan et al. 2018). Furthermore, other radio telescopes, like the Murchison Widefield Array (MWA) (Kaplan et al. 2015), Low Frequency Array (LOFAR) (Fallows et al. 2013), and Square Kilometre Array (SKA) (Nakariakov et al. 2015; Nindos et al. 2019) have also adopted IPS investigations as

* E-mail: ljliu@nao.cas.cn

† E-mail: pb@nao.cas.cn

‡ E-mail: yulei@nao.cas.cn

§ E-mail: bliu@nao.cas.cn

one of their scientific goals.

Observations of IPS can be conducted either by a single station or by multi stations (Armstrong & Coles 1972; Coles & Kaufman 1978; Zhang 2007; Bisi et al. 2010a,b). The four-station system in Japan is a representative of the multi-station system, and it can measure the radial solar wind projection (Asai et al. 1995). Due to some practical reasons, most IPS facilities have adopted the single station system, like the ORT (Manoharan 2010), MWA (Morgan et al. 2018; Chhetri et al. 2018a,b) and the 25m radio telescope in Urumqi, Xinjiang, China (Liu et al. 2010). For the single station observations, two analysis modes are available, dependent on the system observing capabilities, namely the single-frequency (SSSF) analysis mode, and the dual-frequency (SSDF) analysis mode (Zhang 2007). In the single-frequency analysis, the solar wind velocity can be calculated from a multi-parameter model fitting or from the characteristic frequencies of the power spectrum. As for the dual-frequency analysis, the solar wind velocity can be drawn from the first zero-crossing frequency of the normalised co-spectrum (N.C.S).

In China, IPS observations were started in 1990s with the Miyun Synthesis Radio Telescope (MSRT) in Miyun station, which was run by Beijing Astronomical Observatory (BAO), Chinese Academy of Sciences and now is called National Astronomical Observatories, Chinese Academy of Sciences (NAOC) (Ma 1993; Zhang & Wu 2001; Wu et al. 2001), which is an array of 28 single dishes. The effective area of MSRT is equal to a 47m single dish, with the observing frequency of 232 MHz.

An IPS quasi-regular observation system was established with the 25m radio telescope in Urumqi (Liu et al. 2010) in 2008, with a central observing frequency of 1.4GHz. It is the first IPS observation system launched in a single dish in China. The observing frequency of the telescopes in Ooty and Solar-Terrestrial Environment Laboratory, Nagoya University (STELab, which is now called ISEE) are both 327MHz. Since IPS observations can capture distance information corresponding to frequencies, while observing IPS sources at higher frequencies, one can obtain the information relatively closer to the Sun (Scott et al. 1983), therefore the Urumqi telescope can obtain information on approaching position less than 18 solar radii (Zhang 2007).

In 2006 a mega-science project in China was launched, called the Meridian Space Weather Monitoring Project (Meridian Project for short). There is a sub-system of this project to develop ground-based IPS observations, which is configured on the 50m telescope in Miyun station run by NAOC. There are two dual-frequency receivers available in this system, one is centered at 327/611 MHz and the other is centered at 2300/8400 MHz. The bandwidths of the four central frequencies are 40, 40, 300 and 800 MHz respectively. This IPS facility aimed to obtain the solar wind velocity and scintillation index information for space weather forecasting (Zhu et al. 2012). In the near future, an IPS facility will be built in Inner Mongolia for the National Meridian Project 2 (Yan et al. 2018), which is a three-station system with observing frequencies centered at 327 MHz, 654 MHz, and

Table 1. Key observation parameters of ORT and FAST. T_{sys} for FAST is provided for 327 MHz for direct comparison with ORT.

Facility	T_{sys} (K)	A_{eff} (m^2)
ORT	150	8000
FAST	70	49500

1.4 GHz.

The Five-hundred-meter Aperture Spherical radio Telescope (FAST) was constructed successfully in Pingtang country, Guizhou province of China in 2016. In the commissioning phase, some preliminary IPS observations have been carried out. The observation parameters of FAST and ORT (Oberoi 2000) are given in Table 1. According to Table 1, to observe a target source of 1 Jy with an integration time of 1 s with a typical bandwidth of 4 MHz, FAST can achieve a signal-to-noise ratio (S/N) of 95, while the ORT reaches a S/N of 25 with the same settings. Based on the high sensitivity of FAST and the wide frequency coverage of the Ultra-Wideband (UWB) receiver, we can observe weak IPS phenomena within a short time, and analyze the confidence intervals associated to solar wind velocity, which is reported in section 3.

The IPS observation with FAST is introduced in section 2. The data reduction is presented in section 3. Discussions and concluding remarks are then presented in section 4.

2 IPS OBSERVATION WITH FAST

Since 1993, astronomers and engineers from different countries including China have been involved in an ambitious international science project, later referred as the Square Kilometre Array (SKA) with a collecting area of one square kilometer, while the location of FAST was a potential candidate site of the SKA (Peng et al. 1997, 2000b) as the Chinese SKA program (Peng & Nan 2002). FAST is now the largest single-dish radio telescope in the world Fig. 1 (a), with a unique sensitivity to carry out some revolutionary scientific goals, like surveying neutral hydrogen in the universe, detecting the faint and rare types of pulsars, looking for the first shining stars, etc. (Peng et al. 2000a; Nan et al. 2011).

After the first light of FAST observations in September 2016, FAST entered into its commissioning phase. Some calibrators used in the FAST testing phases are IPS sources such as 3C 286 and 3C 279. As a benefit of the big collecting area, FAST has an extraordinary sensitivity, which is shown in Table 1. Compared to other telescopes, the unique high sensitivity of FAST improves the capability of weak signal detection in IPS observations. As a result, a series of IPS experiments were completed successfully by this giant radio telescope.

The aperture diameter of FAST is 500m with the frequency coverage from 70 MHz to 3 GHz. The high-frequency end will be extended to 8 GHz in future upgrades (Nan et al.

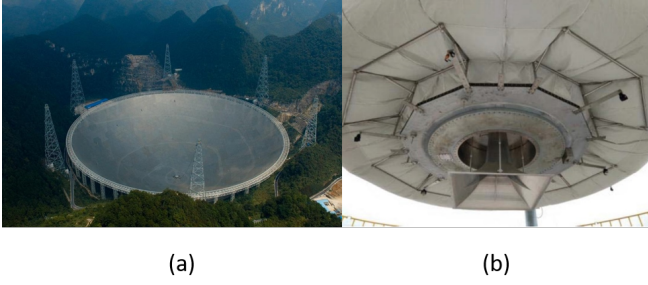


Figure 1. The picture of FAST (a), equipped with the Ultra-Wideband (UWB) receiver (b)

Table 2. Details of observations.

Source	Dates (2017)	Sampling rate (ms)	Duration time (min)
3C 286	11/13, 11/17	0.1	10
3C 279	11/13, 11/18	0.1	10

2011). From July 2016 to May 2018, before the installation of the 19-beam receiver, the Ultra-Wideband (UWB) receiver Fig. 1 (b) was used, by which all IPS data were observed. This receiver covers a frequency range of 270-1620 MHz.

Like other observing systems, the IPS observing system in FAST consists the dish, UWB receiver, digital back-end, and the data processing pipeline. The UWB receiver mounted on FAST has a large bandwidth ratio of 1:6. The wide coverage feature can effectively reduce the number of receivers. The entire bandpass of the Reconfigurable Open Architecture Computing Hardware (ROACH) for data collection is divided into multi-bands, the data quality is flexibly controlled and can be explicitly displayed and checked. In order to obtain both on-source and off-source data, the tracking mode of FAST was taken for our IPS observations.

The FAST UWB receiver has a digital acquisition back-end that includes two polarizations designed for pulsar observation, which is suitable for IPS observations. The sampling interval of 0.1 ms is sufficient for IPS studies. The data acquisition of the UWB receiver is separated equally into two bands. The low-frequency band covers 270-800 MHz and the high-frequency band covers 1200-1620 MHz. Both bands are then divided into multi-channel, and each channel covers a frequency window of 0.25 MHz.

3 DATA REDUCTION

From late 2016 to May 2018, a series of experimental IPS observations were carried out with FAST. After some system testing, debugging and calibration, the IPS observation was firstly making use of the calibration data from FAST to monitor the solar wind. The sources observed, typical sampling rate, the dates and the duration time of the observations are given in Table 2

Equipped with the wideband receiver, observations of

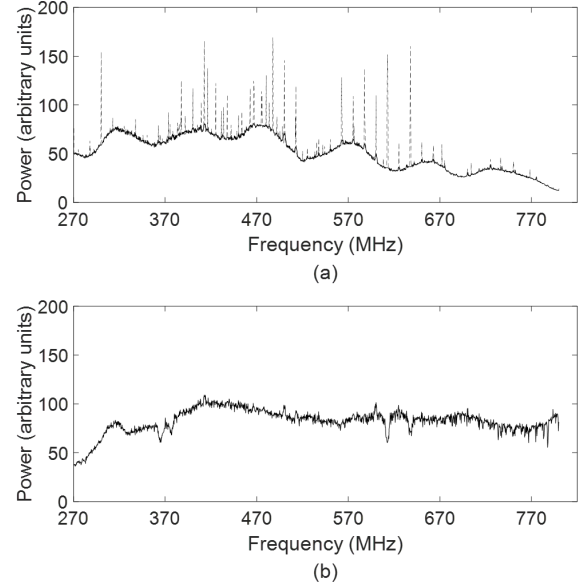


Figure 2. The frequency spectrum of the FAST Ultra-Wideband (UWB) receiver showing a standing-wave pattern. The frequency coverage of this spectrum is 270-800 MHz, with a duration of 20 ms. The target source was 3C 286, and was observed on 13 November 2017. (a) The dashed and solid lines are the frequency-spectrum before and after RFI removal respectively. (b) The normalized spectrum which has eliminated the systematic instrumental response between different frequency.

IPS with FAST can be conducted in both SSSF and SSDF analyses methods simultaneously, which helps us to get the solar wind velocity (V), the anisotropic axial ratio (AR), which is the ratio of the major to the minor axis of the density irregularity (Yamauchi et al. 1998), the spectral index of electron density fluctuation (α) and source size (θ_0) with high precision. During the commissioning phase, the high-frequency band system was not very stable. therefore our discussions are focused on the low-frequency band data.

In this section, the data reduction pipeline and data processing procedure is introduced. Including the choice of IPS observing frequency, bandwidth, the length of time series, and a model-fitting method to obtain the solar wind velocity.

3.1 Data Reduction Pipeline

For IPS data processing, the radio frequency interference (RFI) in the data recorded by the UWB receiver are first removed, to form a new time series which is integrated both on time and frequency.

Fig. 2 demonstrates a data sample of the 270-800 MHz frequency-spectrum collected by the UWB receiver with a duration time of 20 ms. The target source was 3C 286, and was observed on 13 November 2017. In Fig. 2 (a) the dashed and solid lines are the frequency-spectrum before and after RFI removal respectively. Fig. 2 (b) is the normalized spectrum which has eliminated the systematic instrumental response between different frequency. The broad-band fluctuation in the bandpass is probably due to standing

waves, while the strong narrow-band lines are caused by the RFI. It is obvious that, after removing the RFI, the interferences through the whole bandpass are significantly suppressed. For traditional receivers, the acquisition data are summed throughout the whole bandwidth, which will cause some uncertainty to the collected data, therefore, it is essential to remove the RFI. However, the multi-channel design in the FAST UWB receiver in a radio-quiet location allows us to identify the channels with RFI and removed it more effectively.

A general expression of the telescope observed signal is:

$$S_{obs} = S_{sig} + \varepsilon + S_{RFI}. \quad (1)$$

Where S_{obs} is observed signal, S_{sig} is the signal-of-interest(SOI), ε is the additive background white Gaussian noise and S_{RFI} is RFI. We assume that the RMS of the SOI with noise is different from the RFI. As a result of the baseline of the frequency-spectrum is very complicated, we use the rate of change of the SOI rather than the spectrum itself to identify SOI and RFI. Then Random sample consensus (RANSAC) is applied to remove RFI. The main steps are: 1) Initializing the hyperparameters (inner point ratio and tolerance boundary) and fitting model selection (a line model). 2) Convolution of the spectrum with Laplacian of Gaussian filter. 3) Fitting the line model and identify the inner and outer data. 4) Doing average interpolation for the outer data. 5) Repeating the steps 2 to 4 until the RMS of spectrum convergence. The narrow-band RFI can be correctly removed by this method, and based on that, eliminated the relatively wide-band RFI can be achieved by iteratively the method.

The bandwidth of each point of these new data is 10 MHz with an integration time of 20 ms. The data reduction pipeline Fig. 3 is described as follows: 1) The new data set is then divided into some sub-set, with 512 data points and a duration time of about 10 s. Each sub-set is subtracted by its average since the IPS phenomenon only relates to the flux variance. 2) Apply the fast Fourier transform (FFT) to obtain the power spectrum, from which one can extract variance information in frequency scale. The data sample is smoothed using Hanning Window as the Window function so as to reduce the cut-off effects of the FFT. 3) Average the spectrum of 2 sub-set and normalize it to form the SSSF power spectrum of a time duration of 20 s. There is some observational evidence for AR to be close to unity when the solar elongation is larger than 15° (Coles & Kaufman 1978; Yamauchi et al. 1996), that means the low-frequency part of the SSSF power spectrum is almost flat. The elongation of 3C 286 on 13 November 2017 was beyond 30° . So in the following of the paper, the data points of 3C 286 below 0.7 Hz are set to be the same value. The data processing steps 1) to 3) are applied subsequently to the SSSF analysis. The last step is the SSDF analysis based on Scott et al. (1983), which takes the FFT outputs from step 2) to perform auto-correlation and cross-correlation for each dual-frequency pair.

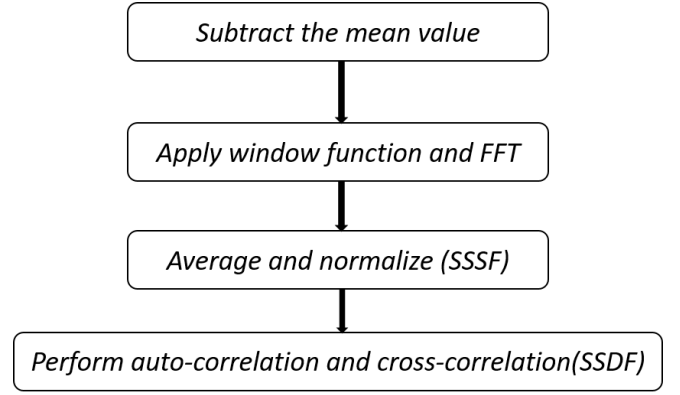


Figure 3. The data reduction pipeline for SSSF and SSDF analyses.

3.2 Data Processing Results

The IPS observation was intended to monitor the solar wind and to calculate the velocity and scintillation index. The UWB receiver is capable of taking data over very wide bandwidths which can be split up and analysed very flexibly thus making it possible to perform both SSSF and SSDF analyses on the same data set simultaneously. Furthermore, any observing frequency bands could be chosen flexibly. Since there was no extra observation time to be applied, calibrators like 3C 286 and 3C 279 are chosen for our IPS study.

The on- and off-source raw data of 3C 286 and 3C 279 observed on 13 November 2017, are shown in Fig. 5 (a) and (b) respectively. The observing frequency is centered at 305 MHz. The fluctuation levels for on- and off-source observations have a significant difference as shown in Fig. 4 (a) and (b). There is obvious discrimination as shown in the two rectangles in Fig. 4 (a). While in Fig. 4 (b), the fluctuations in the two rectangles are at a similar level. Which can also be reflected by the RMS values. So the scintillation level of 3C 286 that day was stronger than that of 3C 279. In the following, the results derived from the observation on 3C 286 are discussed as an example.

Fig. 5 demonstrates the SSSF analysis mode power spectrum of the source 3C 286 observed on 13 November 2017. The central frequencies for Fig. 5 (a) and (b) are 305 MHz and 715 MHz, respectively, and each of which has a bandwidth of 10 MHz. Fig. 5 clearly shows that the power spectrum at 305 MHz has a higher scintillation level than the spectrum at 715 MHz. According to equation (2), the scintillation index m (Cohen et al. 1967) is 0.09 for the low frequency and 0.08 for the high frequency, where C_{on} (C_{off}) is the average intensity of the on-source (off-source) signal, and σ_{on}^2 (σ_{off}^2) is the square of the RMS of intensity scintillation.

$$m = \frac{\sqrt{\sigma_{on}^2 - \sigma_{off}^2}}{C_{on} - C_{off}}. \quad (2)$$

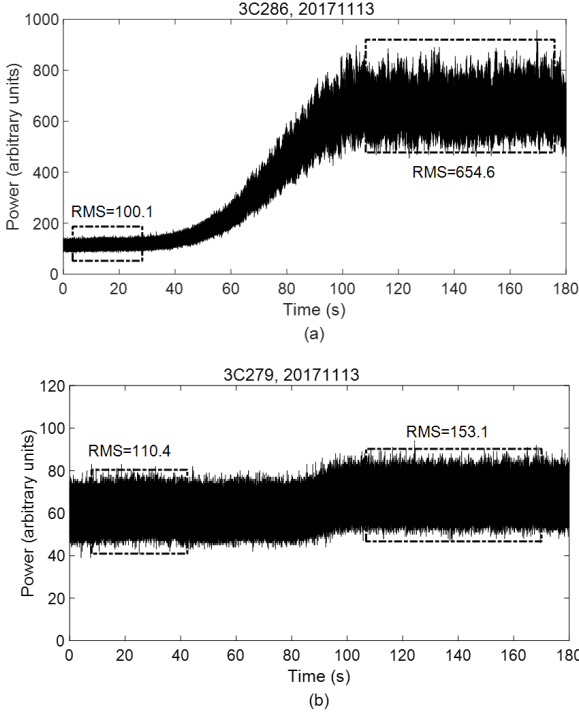


Figure 4. The off-(on) raw data of 3C 286 (a) and 3C 279 (b) observed at 305 MHz on 13 November 2017, respectively, the four rectangles present the fluctuations of on-source and off-source.

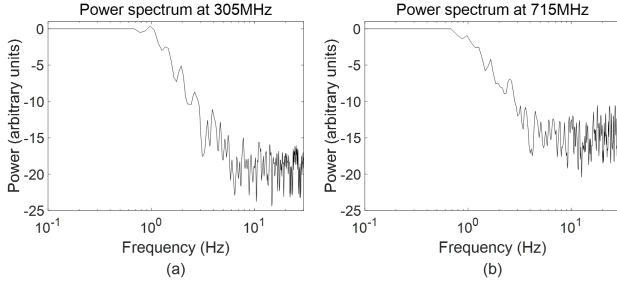


Figure 5. SSSF analysis mode power spectra for 3C 286 at 305 MHz and 715 MHz on 13 November 2017.

3.3 Model-fitting

The solar wind velocity from SSSF analysis can be obtained either by 1) the characteristic frequency called Fresnel knee frequency or 2) by model fitting via some parameters. In equation (3) (Scott et al. 1983), V stands for the solar wind velocity, f_F the Fresnel knee frequency, z the distance to the scattering screen, and λ the wavelength of the observing frequency;

$$V = f_F \sqrt{z \lambda \pi}. \quad (3)$$

In the case of the model-fitting theoretical model used for SSSF analysis mode is given for the weak scintillation region, the formula can be represented by a theoretical temporal power spectrum $P(f)$ which is shown in equation (4), where f is the temporal frequency, $C = (2\pi r_e \lambda)^2$ is a con-

stant related to observing wavelength λ , and r_e is the electron radius.

$$P(f) = C \int_{-z}^z \frac{1}{V_p(z)} dz \int_{-\infty}^{+\infty} \Phi_{ne} F_{diff} F_{source} dq_y. \quad (4)$$

In equation (4), the spectrum of the electron-density fluctuations $\Phi_{ne} \propto q^{-\alpha}$, where $q = \sqrt{q_x^2 + q_y^2 + q_z^2}$ is the three-dimensional wave number. F_{diff} is the Fresnel propagation filter and F_{source} is the squared modulus of the source visibility (Manoharan & Ananthakrishnan 1990; Mejia-Ambroz et al. 2015; Chang et al. 2019).

In some previous studies, the fitting parameters like AR and α are often set to be a fixed number for simplicity, and only to do the model-fitting (Oberoi 2000) by adjusting the solar wind velocity V . In our IPS studies, a numerical optimization applies a weighted trust-region reflective least square (TRRLS) algorithm to optimize the four parameters (including V , AR , α , and source size of the radio source) of IPS model, which are based on the physical constraints. The fitting parameters are obtained via fitting the theoretical model to the actual power spectrum. We used the 95% confidence intervals as the error bars of the parameters. Moreover, the multi-initialization strategy applied will guarantee the fitting convergence in the global minimization. In order to obtain a good performance in the fitted velocity, we used the weighted nonlinear least-square fitting. The objective function of this method is:

$$\min \frac{1}{N_m} \sum_{i=1}^{N_m} W(i) \|\lg(P_m(V, AR, \alpha, \theta_0)) - \lg(P_{obs})\|_2^2. \quad (5)$$

where N_m is the number of points which will be used to carry out model-fitting, W is weight, $P_m(V, AR, \alpha, \theta_0)$ and P_{obs} are the IPS model and observed power spectra, respectively.

Fig. 6 shows some examples of the SSSF model-fitting results of 3C 286 with different time lengths, and the central observing frequency is set to be at 285 MHz. The solid and dashed lines show the observed and model-fitting spectrum respectively. The time length of the power spectrum of Fig. 6 (a), (b) and (c) is 20 s, and that of Fig. 6 (d) is 300 s. Table 3 are the parameters with error bars obtained by a data set of 300 s, each velocity is obtained with a 20 s time length. The corresponding value for data with 300 s are: $V = 598.2 \pm 10.2 \text{ km/s}$, $AR = 1.1 \pm 0.3$, $\alpha = 2.7 \pm 0.5$, source size = $0.03 \pm 0.03''$. The weighted mean value with scatter for each column of Table 3 are: $V = 620.9 \pm 4.1 \text{ km/s}$, $AR = 1.1 \pm 0.1$, $\alpha = 2.8 \pm 0.2$ and source size = $0.04 \pm 0.01''$. According to ISEE, the solar wind velocity obtained from observations of 3C 286 on 14 November 2017 was 609 km/s. It can be concluded that resulting solar wind velocity with the data of 20 s integration is consistent with the ones with the time length of 300 s. That means the model-fitting method developed is applicable, therefore, with the high sensitivity of FAST, the solar wind velocity can be derived from a 20 s observation for this source that day.

The low-frequency band of FAST UWB receiver covers a wide frequency range from 270 to 800 MHz, which is

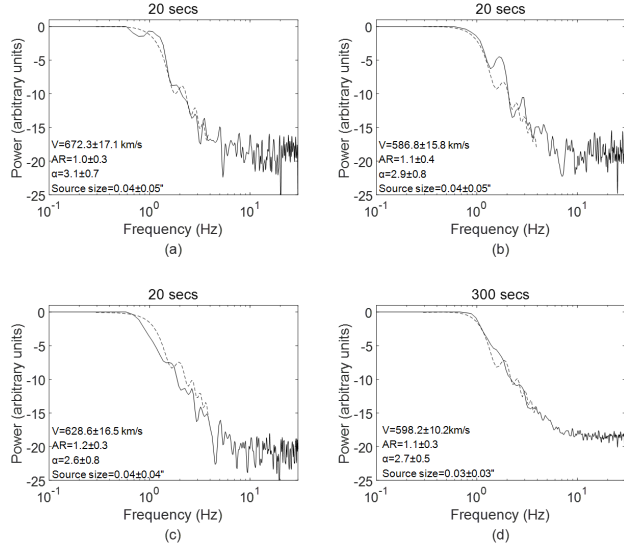


Figure 6. The model-fitting example of source 3C 286 with SSSF analysis mode, the central observing frequency is 285 MHz. The solid and dashed lines show the observed and fitting spectra respectively. (a), (b), (c) are the results for the time length of 20 s, and (d) is that of 300 s.

Table 3. Shown here are the fitted parameters with error bars for the 300 s observation divided up into 20 s intervals using the SSSF analysis method on the central frequency of 285 MHz with a 10 MHz bandwidth. We used the 95% confidence intervals as the error bars of the parameters. The last row demonstrates the weighted mean values with scatter for each column.

V (km/s)	AR	α	Source size (arcsec)
626.2±14.5	1.1±0.4	2.7±0.7	0.04±0.04
636.4±17.5	1.1±0.3	2.8±0.8	0.04±0.05
552.4±11.4	1.1±0.2	3.0±0.5	0.01±0.09
672.3±17.1	1.0±0.3	3.1±0.7	0.04±0.05
623.3±20.6	1.1±0.4	2.9±0.7	0.01±0.12
663.4±18.2	1.0±0.3	3.3±0.8	0.01±0.19
586.8±15.8	1.1±0.4	2.9±0.8	0.04±0.05
749.1±17.1	1.0±0.3	3.1±0.7	0.04±0.05
577.2±20.6	1.0±1.0	1.6±0.9	0.04±0.05
628.6±16.5	1.2±0.3	2.6±0.7	0.04±0.04
624.7±14.7	1.0±0.4	2.7±0.6	0.04±0.04
647.6±13.1	1.0±0.3	3.3±0.5	0.01±0.14
579.5±11.9	1.0±0.4	2.5±0.5	0.04±0.03
560.7±14.6	1.1±0.5	2.4±0.7	0.04±0.04
642.3±22.9	0.9±0.7	1.8±1.2	0.07±0.05
620.9±4.1	1.1±0.1	2.8±0.2	0.04±0.01

divided into 53 sub-bands, and each sub-band covers a frequency of 10 MHz. Fig. 7 shows the results of the four fitting parameters (V , AR, α , and source size) obtained from each sub-band, the bands those affected by strong RFI are rejected. The time length for each result is 20 s. The stars and solid lines are the fitting values and the error bars respectively.

The mean velocity in Fig. 7 is 531.9 km/s with a standard

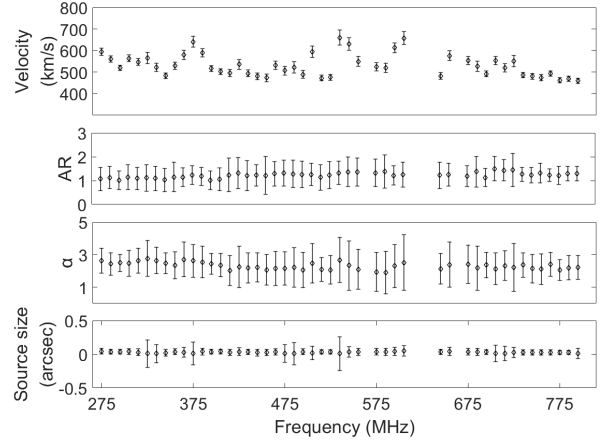


Figure 7. The solar wind parameters from the 10 MHz bandwidth sub-bands using 20 s time length. From top to down, the four parameters, velocity, AR, α , and source size. The sub-bands affected by strong RFI are rejected. The stars and solid lines represent the fitting values and the error bars.

Table 4. SSSF and SSDF analyses modes velocity results with a duration time of 300 s. The 1-3 columns are the frequency, velocity, and error, respectively.

Frequency (MHz)	Velocity (km/s)	Error (km/s)
305	593.4	10.2
715	465.0	7.3
305/715	747.8	-

deviation of 52.7 km/s, revealing velocity estimates from about 600 km/s at lower frequency to ~ 450 km/s at higher frequency, with a fractional variability of $\sim 9.9\%$ over a frequency range of ~ 500 MHz, mostly in linear trend. The model-fitting values of AR, alpha, and the source-size component tend towards constants, which can also confirm that why some former studies set these three parameters in a fixed number (e.g. Oberoi 2000). That means the parameters obtained from the model-fitting methods are reliable, and the new telescope FAST has very good advantages for investigating the inner heliosphere with IPS using both analyses types.

For SSDF analysis mode, the solar wind velocity is deduced from the first zero-crossing frequency of the N.C.S. In equation (6) λ_1 is the wavelength of the lower observing frequency, z is the effective screen distance, f_{zero} is the first zero-crossing frequency of N.C.S, A is a correcting factor which varies slightly with the solar wind parameters and is always set to a constant, 1 (Scott et al. 1983; Tokumaru et al. 1994; Zhang 2007).

$$V = A f_{zero} \sqrt{z \lambda_1}. \quad (6)$$

Fig. 8 shows the result of the SSDF spectrum of 3C 286 observed on 13 November 2017. The two observing frequencies are 305 MHz and 715 MHz. The time length of the dataset

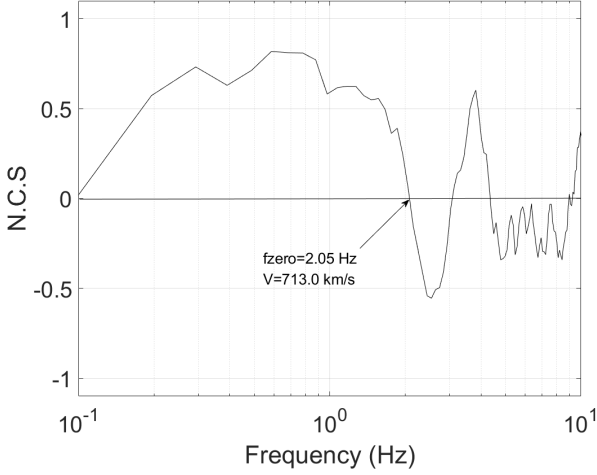


Figure 8. The power spectra of source 3C 286 in SSDF analysis modes, which is observed on 13 November 2017. The two frequencies adopted here are 305 MHz and 715 MHz. The time length of this data set is 20 s, and the arrow shows the f_{zero}

is 20 s and the arrow shows the first crossing frequency f_{zero} of the N.C.S. which is 2.05 Hz, and the deduced solar wind velocity is 713.0 km/s. The velocities at the same time length from the SSSF analysis mode are 564.4 ± 16.5 km/s (305 MHz) and 554.2 ± 19.6 km/s (715 MHz) taken from Fig. 7, which is consistent with the velocity variation trend observed in Fig. 7. Table 4 presents the velocity results of SSSF and SSDF analyses modes with a duration time of 300 s. From column 1-3 shows the frequency, velocity, and error, respectively. It can be seen that the velocities deduced from 20 s are consistent with the results of 300 s. The velocity deduced from SSDF analysis mode is likely to be affected by the random velocity (Tokumaru et al. 1994), that may be the reason why the velocity of SSDF is higher than the velocity obtained from SSSF analysis mode. Or may be that the IPS is weak at that time, so the reliability of the velocity determination is reduced. But the cause of the difference of velocity still needs further study.

4 DISCUSSIONS AND CONCLUDING REMARKS

There are four remarkable advantages to carry out IPS observations with the newly established telescope FAST. Firstly, FAST is incredibly sensitive to search for weak signals owing to its unique huge collecting area, which allows us to obtain the solar wind velocity information in a short observation of ~ 20 s. Since the IPS is a fast-changing phenomenon with a timescale of ~ 1 s (Cohen 1969), the long integration is likely to obscure the scintillation phenomena. Secondly, the bandwidth can be chosen flexibly. Otherwise, if the adopted bandwidth is larger than the coherence scales, the scintillation will be smeared because the IPS is a frequency-dependent phenomenon (Little 1968). Thirdly, with the wide frequency coverage of the receiver and multi-channels, IPS observations in SSSF and SSDF

Table 5. The effect of different Δf . Column 1-5 shows the f_1 , f_2 , Δf , f_{zero} and V respectively

f_1 (MHz)	f_2 (MHz)	$\Delta f = f_2 - f_1$ (MHz)	f_{zero} (Hz)	V (km/s)
285	335	50	3.516	1265.1
285	385	100	2.148	772.9
285	435	150	2.051	737.9
285	485	200	2.051	737.9
285	535	250	2.051	737.9
285	585	300	2.051	737.9
285	635	350	2.051	737.9
285	685	400	2.148	772.9
285	735	450	2.051	737.9
285	785	500	2.051	737.9

analysis modes can be conducted with FAST simultaneously. The velocities derived from the two analysis modes provide a good supplement. In addition, IPS studies do not require large extra and dedicated observing time, for if the position of the source is appropriate we can take most calibrators as IPS targets which accommodate a symbiotic project.

Because of the wide frequency coverage of the UWB receiver, we can also study the effect of different frequency difference of SSDF analysis mode. Table 5 shows the result of the comparison of different frequency differences Δf ($\Delta f = f_2 - f_1$). f_1 in Table 5 is set to be 285 MHz. The five columns are two observing frequencies, Δf , the first zero-crossing frequency and the deduced solar wind velocity. It can be concluded from Table 5 that, when Δf is bigger than 30% of f_1 , then the deduced f_{zero} is tend to be stable. The reason of this frequency differences still request some follow up study.

Our preliminary results demonstrated that FAST has an outstanding potential to perform observations of IPS. By comparing the solar wind velocities calculated from the SSDF and SSSF analysis modes, the reliability of observation is proven. In general, taking advantage of the high sensitivity and wide frequency coverage as well as the multi-channel design of the UWB receiver, the observation time with FAST can significantly decrease on each IPS source, and the choice of frequencies is flexible to get rid of the RFI contaminated data.

We conclude that a larger number of target sources can be observed with FAST on a short time scale. therefore, the IPS data from FAST will widen the range of Solar-terrestrial space and improve the accuracy of estimation of solar wind velocity. This can be further utilized in space weather forecasts.

ACKNOWLEDGEMENTS

This work is supported by the National Key R&D Program of China under grant number 2018YFA0404703, and the Open Project Program of the CAS Key Laboratory of FAST, NAOC, Chinese Academy of Sciences. Basic research program and project of Yunnan province of China

(2019FB009). The authors thank all the staff of JLRAT, NAOC, for their help during the observations. We are grateful to Yu-Hai Qiu, Xi-Zhen Zhang, Cheng-Min Zhang, Ming Xiong (National Space Science Center, CAS), R. A. Fallow (ASTRON), M. Tokumaru (Solar-Terrestrial Environment Laboratory, Nagoya University, Nagoya, Japan) and Julio Mejia-Ambriz (SCiESMEX, Instituto de Geofísica, Unidad Michoacan, Universidad Nacional Autónoma de México), for their helpful discussions. The authors also thank Yue Ma and Sivasankaran Srikanth (National Radio Astronomy Observatory, NRAO), for their help to polish the English. O. C. acknowledges the European Union Horizon 2020 research and innovation program under the Marie Skłodowska-Curie grant agreement 665593 awarded to the Science and Technology Facilities Council. M. M. B. acknowledges STFC in-house research funding to RAL Space under the STFC Astronomy Grants Panel Consolidated Grants Programme. This work made use of the data from FAST (Five-hundred-meter Aperture Spherical radio Telescope). FAST is a Chinese national mega-science facility, operated by the National Astronomical Observatories, Chinese Academy of Sciences.

DATA AVAILABILITY

The raw data underlying this article cannot be shared publicly due to the data policy of FAST. The intermediate process data will be shared on reasonable request to the corresponding author.

REFERENCES

- Armstrong J. W., Coles W. A., 1972, *J. Geophys. Res.*, **77**, 4602
- Asai K., Ishida Y., Kojima M., Maruyama K., Misawa H., Yoshimi N., 1995, *Journal of geomagnetism and geoelectricity*, **47**, 1107
- Bisi M. M., Fallows R. A., Breen A. R., O'Neill I. J., 2010a, *Sol. Phys.*, **261**, 149
- Bisi M. M., et al., 2010b, *Sol. Phys.*, **265**, 49
- Chang O., Gonzalez-Esparza J. A., Mejia-Ambriz J., 2016, *Advances in Space Research*, **57**, 1307
- Chang O., Bisi M. M., Aguilar-Rodriguez E., Fallows R. A., Gonzalez-Esparza J. A., Chashei I., Tyul'bashev S., 2019, *Space Weather*, **17**, 1114
- Chhetri R., Morgan J., Ekers R. D., Macquart J. P., Sadler E. M., Giroletti M., Callingham J. R., Tingay S. J., 2018a, *MNRAS*, **474**, 4937
- Chhetri R., Ekers R. D., Morgan J., Macquart J. P., Franzen T. M. O., 2018b, *MNRAS*, **479**, 2318
- Clarke M. E., 1964, PhD thesis, Cambridge University
- Cohen M. H., 1969, *ARA&A*, **7**, 619
- Cohen M., Gundermann E., Hardebeck H., Sharp L., 1967, *The Astrophysical Journal*, **147**, 449
- Coles W., Kaufman J., 1978, *Radio Science*, **13**, 591
- Fallows R. A., Asgekar A., Bisi M. M., Breen A. R., ter-Veen S., 2013, *Sol. Phys.*, **285**, 127
- Hewish A., Symonds M., 1969, *Planetary and Space Science*, **17**, 313
- Hewish A., Scott P., Wills D., 1964, *Nature*, **203**, 1214
- Kaplan D. L., et al., 2015, *ApJ*, **809**, L12
- Little L., 1968, *Planetary and Space Science*, **16**, 749
- Liu L.-J., Zhang X.-Z., Li J.-B., Manoharan P., Liu Z.-Y., Peng B., 2010, *Research in Astronomy and Astrophysics*, **10**, 577
- Ma G. Y., 1993, PhD thesis, Beijing Astronomical Observatory, Chinese Academy of Sciences
- Manoharan P. K., 2010, *Sol. Phys.*, **265**, 137
- Manoharan P., Ananthakrishnan S., 1990, *Monthly Notices of the Royal Astronomical Society*, **244**, 691
- Mejia-Ambriz J. C., Villanueva-Hernandez P., Gonzalez-Esparza J. A., Aguilar-Rodriguez E., Jeyakumar S., 2010, *Sol. Phys.*, **265**, 309
- Mejia-Ambriz J. C., Jackson B. V., Gonzalez-Esparza J. A., Buffington A., Tokumaru M., Aguilar-Rodriguez E., 2015, *Sol. Phys.*, **290**, 2539
- Morgan J. S., et al., 2018, *MNRAS*, **473**, 2965
- Nakariakov V., et al., 2015, in *Advancing Astrophysics with the Square Kilometre Array (AASKA14)*. p. 169 ([arXiv:1507.00516](https://arxiv.org/abs/1507.00516))
- Nan R., et al., 2011, *International Journal of Modern Physics D*, **20**, 989
- Nindos A., Kontar E. P., Oberoi D., 2019, *Advances in Space Research*, **63**, 1404
- Oberoi D., 2000, PhD thesis, Department of Physics Indian Institute of Science
- Peng B., Nan R., 2002, *The Radio Science Bulletin*, **300**, 12
- Peng B., Nan R., Qiu Y., Nie Y., Zhu B., Xu X., Strom R., 1997, *Further site survey for the next-generation large radio telescope in Guizhou*. Cambridge University Press, Cambridge, UK, p. 278
- Peng B., Strom R. G., Nan R., Ma E., Ping J., Zhu L., Zhu W., 2000a, in van Haarlem M. P., ed., *Perspectives on Radio Astronomy: Science with Large Antenna Arrays*. p. 25
- Peng B., Nan R., Su Y., 2000b, in Butcher H. R., ed., *Society of Photo-Optical Instrumentation Engineers (SPIE) Conference Series Vol. 4015, Radio Telescopes*. pp 45–54, [doi:10.1117/12.390439](https://doi.org/10.1117/12.390439)
- Scott S. L., Rickett B. J., Armstrong J. W., 1983, *A&A*, **123**, 191
- Tokumaru M., Kondo T., Mori H., Tanaka T., 1994, *Journal of Geomagnetism and Geoelectricity*, **46**, 835
- Wu J., Zhang X., Zheng Y., 2001, *Ap&SS*, **278**, 189
- Yamauchi Y., et al., 1996, in Winterhalter D., Gosling J. T., Habal S. R., Kurth W. S., Neugebauer M., eds, *American Institute of Physics Conference Series Vol. 382, American Institute of Physics Conference Series*. pp 366–366, [doi:10.1063/1.51472](https://doi.org/10.1063/1.51472)
- Yamauchi Y., Tokumaru M., Kojima M., Manoharan P. K., Esser R., 1998, *J. Geophys. Res.*, **103**, 6571
- Yan Y., Wang W., Chen L., Liu F., Geng L., Chen Z., 2018, *Sun and Geosphere*, **13**, 153
- Zhang X.-Z., 2007, *Chinese J. Astron. Astrophys.*, **7**, 712
- Zhang X. Z., Wu J. H., 2001, in Brekke P., Fleck B., Gurman J. B., eds, *IAU Symposium Vol. 203, Recent Insights into the Physics of the Sun and Heliosphere: Highlights from SOHO and Other Space Missions*. p. 580
- Zhu X.-Y., Zhang X.-Z., Zhang H.-B., Kong D.-Q., Qu H.-P., 2012, *Research in Astronomy and Astrophysics*, **12**, 857

This paper has been typeset from a \LaTeX file prepared by the author.